metals

Article

Stress Intensity Factors and *T*-Stress Solutions for 3D Asymmetric Four-Point Shear Specimens

Mark Cohen and Xin Wang *

Department of Mechanical and Aerospace Engineering, Carleton University, Ottawa, ON K1S 5B6, Canada; mark.e.cohen@outlook.com
* Correspondence: xin.wang@carleton.ca

Abstract: In this paper, extensive three-dimensional finite element analysis is conducted to study an asymmetric four-point shear (AFPS) specimen: a widely used mixed-mode I/II fracture test specimen. Complete solutions of fracture mechanics parameters K_I, K_{II}, K_{III}, T_{11}, and T_{33} have been obtained for a wide range of a/W and t/W geometry combinations. It is demonstrated that the thickness of the specimen has a significant effect on the variation of fracture parameter values. Their effects on the crack tip plastic zone are also investigated. The results presented here will be very useful for the toughness testing of materials under mixed-mode loading conditions.

Keywords: fracture toughness; mixed-mode loading; stress intensity factor; *T*-stress; asymmetric four-point shear specimen

Citation: Cohen, M.; Wang, X. Stress Intensity Factors and *T*-Stress Solutions for 3D Asymmetric Four-Point Shear Specimens. *Metals* **2022**, *12*, 1068. https://doi.org/10.3390/met12071068

Academic Editor: Alberto Campagnolo

Received: 20 May 2022
Accepted: 20 June 2022
Published: 22 June 2022

1. Introduction

The critical value of stress intensity factor, known as K_{IC} or fracture toughness, provides a means to test materials and geometric predisposition to resist fracture. The most common test specimens to determine K_{IC} are specimens loaded by pure mode I loading, such as single-edge notch beam and compact tension specimens. These specimens are often used to represent idealized cases of plane strain fracture under pure mode I loading. A cracked body can, however, be loaded in any number of combinations of three primary loading directions, or modes. In order to determine the onset of fracture for the other modes of loading, and combinations thereof, fracture specimens for mixed-mode loading cases have been developed.

One such specimen, and the focus of this work, is the asymmetric four-point shear (AFPS) specimen described by He, Cao, and Evans [1] (see Figure 1). Note that the distance between crack line and the loading points is defined as offset c; the case of $c = 0$ is shown in Figure 1. This specimen is used to test fracture behaviour under pure mode II (also called antisymmetric four-point shear, or simply four-point shear (FPS) specimen), when the offset $c = 0$ and mixed-mode I/II (called AFPS specimen) loading when the offset c is not zero. Different mixed-mode I/II loading is achieved by varying offset value c. Figure 2a,b illustrated these two cases, respectively.

The AFPS specimen has since been used to test fracture behaviour for mixed mode I/II loading, and 2D solutions were provided by He, Cao, and Evans [1] and later refined by He and Hutchinson [2]. The fracture cases considered by these researchers are simplified by either plane stress or plane strain conditions, where the values of K_I and K_{II} are used as the critical fracture parameters. In all these analyses, the effect of K_{III} is neglected.

In recent studies, 3D finite element analysis has been used to study the effects of finite thickness on fracture behaviour. In order to account for specimen thickness in the interpretation of fracture testing results, comprehensive stress intensity factor (SIF) solutions for varying specimen thicknesses are needed. Researchers such as Jin and Wang [3], Kwon and Sun [4], and Nakamura and Parks [5] have looked at the finite-thickness effect for pure mode I or mode II fracture specimens. Recently, Jin et al. [6] studied the mixed-mode compact-tension-shear (CTS) specimen, and the finite thickness effect was also studied. When considering specimens such as AFPS in 3D, it is therefore expected that all three modes of stress intensity factors, K_I, K_{II} and K_{III}, will be present. No detailed analysis was available until recently.

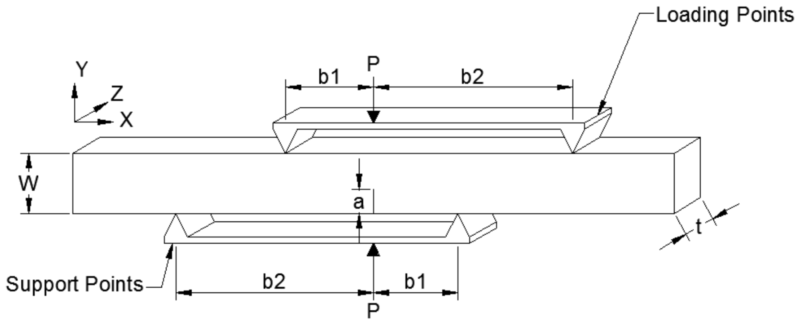

Figure 1. The asymmetric four-point-shear (AFPS) specimen.

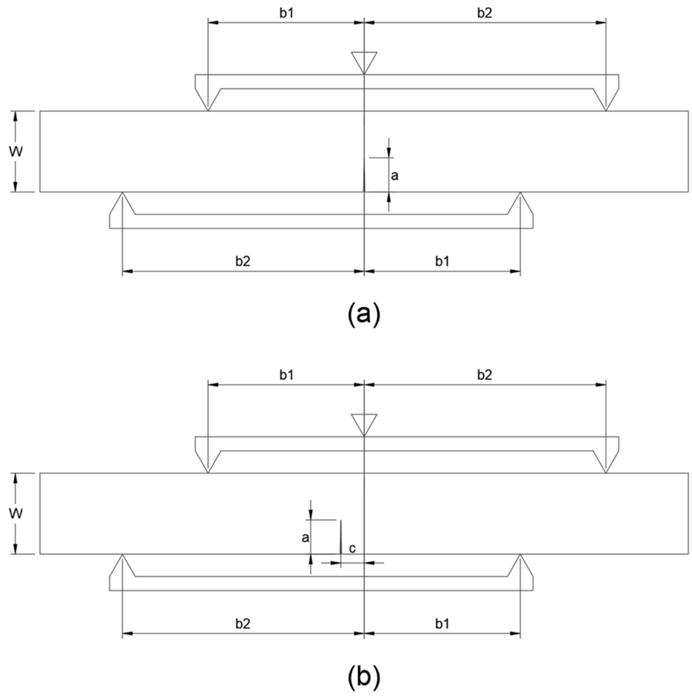

Figure 2. Asymmetric four-point-shear (AFPS) specimen: (**a**) $c = 0$ (**b**) $c \neq 0$.

To help better understand the stress field surrounding the crack tip, the plastic zone can be calculated for given K values. This type of plastic zone analysis determines the plastic zone shape and size for different mixed-mode cases, and is a useful indicator of crack tip stress. By considering specimens in 3D, any variation of the plastic zone along the crack front can be seen.

Traditional fracture testing of mode I specimens yields a value of K_{IC} that is applicable for situations of high crack tip constraint, which may be overly conservative. A number of researchers have shown that it is necessary to include an additional non-singular term in the Williams expansion to adequately describe the stress state surrounding the crack. This non-singular term is known as the T-stress, and forms the basis of the two-parameter fracture mechanics approach, see Betegon and Hancock [7], O'Dowd and Shih [8], and Wang [9], for example. Recently, it has been demonstrated that both in-plane T-stress T_{11} and out-of-plane T_{33} are required to quantify the in-plane and out-of-plane constraint effect [10–12].

In addition, researchers have investigated the effects of *T*-stress magnitude on the plastic zone, for various mixed-mode cases [13]. The *T*-stress values for mode I test specimens have been studied, but calculated values for the mixed-mode AFPS specimen are not readily available.

In this paper, AFPS specimens are studied for a wide variety of plate thicknesses and crack depths. The resulting fracture parameter solutions are presented and used to predict the size and shape of the plastic zone at various locations through the specimen's thickness.

2. Finite Element Model of AFPS Specimen

In this section, the FEA of 3D AFPS specimens is presented.

2.1. 3D FEA Model

The mixed-mode specimen, the AFPS, combines mode II in-plane shear loading with mode I opening (or bending) loading by offsetting the crack location, setting up asymmetric loading. The amount of mode I contribution is controlled by the value of c/W, or the crack offset ratio. Figure 1 depicts the AFPS specimen. In the present paper, the results for $c/W = 0$ and 0.1 will be presented. In Figure 2a,b, the cases of different c values are illustrated.

Geometric parameters were varied in the models created for the mixed mode I/II case: crack length-to-width ratios of $a/W = 0.1$, 0.2, 0.3, 0.4, 0.5, 0.6, and 0.7; and thickness-to-width ratios of $t/W = 0.1$, 0.2, 0.5, 1.0, 2.0, and 4.0.

The material was considered to be perfectly elastic, with an elastic modulus of 207GPa and Poisson's ratio (v) of 0.3, common values for typical engineering materials. An individual case was performed for a value of $v = 0$ and a thickness ratio $t/W = 4.0$, to be used as a representative 2D case.

The mesh design was a constant 2D mesh across the face of the plate (in the x–y direction, see Figure 3), and was swept along the crack front (z direction). The mesh was refined around the loading and boundary condition locations, as well as at the crack tip. The element type throughout the model was a 20-noded quadratic element with reduced integration (C3D20R). At the crack tip, one edge of the element was collapsed to form a wedge with the point at the crack. The mesh refinement around the crack tip was done using 30 elements angularly around the crack tip (Dassault Systems/ SIMULIA, 2013) [14]. Mid-side nodes on the element sides directly adjacent to the crack tip were moved to the quarter point, to better capture the singularity at the crack tip. A typical specimen mesh for a plate with $t/W = 1.0$ and $a/W = 0.1$ is shown in Figure 3, and the C3D20R schematic is shown in Figure 4. Through-thickness, between 20 and 50 elements were used to calculate fracture parameters.

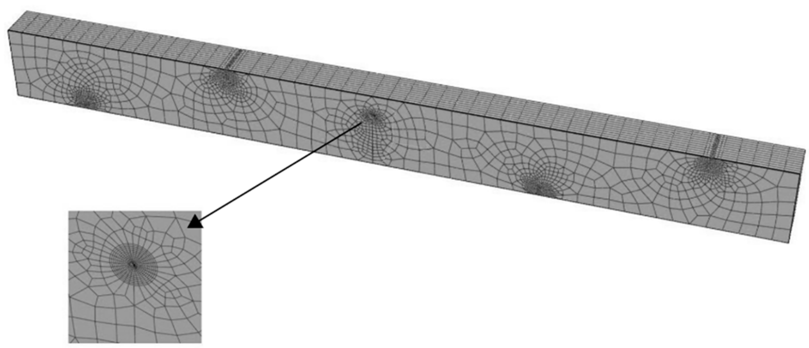

Figure 3. Typical mesh for the AFPS specimen with $a/W = 0.7$, $c/W = 0.1$, and $t/W = 1.0$.

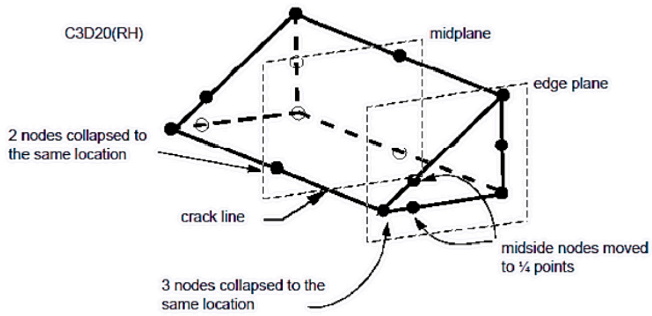

Figure 4. C3D20R element configuration (Dassault Systèmes/SIMULIA, 2013, data from ref. [14]).

Similar meshes were created for each geometric case considered. Many different models were created, with varying numbers of elements from 10,000 to close to 500,000, depending on thickness and crack depth. Mesh convergence studies were performed to ensure the FEA results had converged.

The mesh was refined in two ways: along the thickness direction, the mesh was refined towards the free edge (see Figure 4); and around the crack tip, the mesh was altered to meet the sizing recommended by Abaqus training documentation (Dassault Systems/ SIMULIA, 2013) [14]. Additionally, the mesh was refined around the loading and support points to minimize any potential impact on the crack tip elements.

2.2. Loads and Boundary Conditions

As seen in Figure 3, load P was applied to the upper loading points while the lower support points were restrained. The value of P was set, and the force was distributed two-thirds and one-third to the points as shown in the same figure. The load used for each was a function of the plate thickness, where force P was applied as force/unit length. The value of P selected was 525 N/mm, corresponding to 175 N/mm and 350 N/mm applied to each of the two loading points (on top), respectively. Static loading cases were studied here.

The lower support points were modeled as simple supports, and a single node at the bottom corner of the specimen was restrained from displacing along the length direction, preventing the specimen from having excessive displacement during the analysis.

Both the loading and support points were modeled by applying a pressure or restraining a small strip. The additional mesh refinement helped distribute the stress and deformation across many elements, relieving some of the stress spikes that can occur due to local boundary conditions and loads.

Symmetry was used to simplify the calculation analysis. The midplane (z/t = 0) was chosen as the plane of symmetry, which had an insignificant effect on the results. All results were symmetric about the mid plane, with the exception of K_{III}, which was anti-symmetric.

2.3. Determination of SIF and T-Stress

The FEA models were analyzed using Abaqus built-in contour integral calculation, which modified the crack tip mesh with collapsed element edges, forming degenerate cube (wedge) elements. A diagram of the element design around the crack tip is shown in Figure 4. Abaqus calculated SIF values for each node along the crack tip. Five contours were used for the calculation, and the average of the outer three is presented as the result. For all geometries, convergence of the contour integral indicated that adequate meshing refinement was met, as values were stable after the first two contours.

These results were then extracted from the output files (.dat and .odb) and processed through the use of MATLAB scripts. Using scripted calculations, the results were organized, normalized, and plotted. The expressions used to normalize the results are described in Section 3.1.

Two-dimensional and 3D FEA models were created in Abaqus to reproduce the 2D results presented by He and Hutchinson [2] for the four-point shear specimen. Results will be shown in Section 3. Verification of this kind served to confirm the modelling and calculation techniques that were used to produce the results.

3. SIF and T-Stress Results

To provide a more generalized form of the SIF and T-stress solutions, the results of these parameters are normalized as functions of geometry and loading.

3.1. SIF Normalizing Functions

He and Hutchinson [2] provide the mode I and II stress intensity factors as functions of crack and loading geometry. In a mixed-mode I/II case, K_I can be described as a function of crack and loading geometry:

$$K_I^R = \frac{6cQ}{W^2}\sqrt{\pi a}F_I(a/W) \tag{1}$$

where F_I is the normalized mode I SIF, a function of crack depth and geometry. K_{II} and K_{III} are defined as follows:

$$K_{II}^R = \frac{Q}{W^{\frac{1}{2}}}\frac{(a/W)^{\frac{3}{2}}}{(1-a/W)^{\frac{1}{2}}}F_{II}(a/W) \tag{2}$$

$$K_{III}^R = \frac{Q}{W^{\frac{1}{2}}}\frac{(a/W)^{\frac{3}{2}}}{(1-a/W)^{\frac{1}{2}}}F_{III}(a/W) \tag{3}$$

where F_{II} and F_{III} are the normalized mode II and III SIFs, and Q is shear force, calculated as follows:

$$Q = P(b_2 - b_1)/(b_2 + b_1) \tag{4}$$

3.2. T-Stress Normalizing Functions

The first non-singular term in the Williams expansion is known as T-stress, and the non-zero components can be described as:

$$T_{11} = T \tag{5}$$

$$T_{33} = Ee_{33} + vT \tag{6}$$

It is typical, in 2D and 3D cases, for T-stress to be normalized with respect to the loading, or far-field stress. In the case of the AFPS specimen, the loading stress associated with T-stress comes from the mode I bending stress. The normalizing factor for the T-stress is introduced as σ^{nom}, the nominal bending stress, and is calculated as follows:

$$\sigma^{nom} = \frac{6cQ}{W^2} \tag{7}$$

The normalized T-stress values are presented as

$$T_{11} = \frac{T_{11}}{\sigma^{nom}} \tag{8}$$

$$T_{33} = \frac{T_{33}}{\sigma^{nom}} \tag{9}$$

3.3. SIF and T-Stress Results and Discussion

In order to verify the modelling techniques used to calculate the mixed-mode fracture parameters, results from the current work are compared with literature solutions. Two-dimensional FEA is first performed to verify the expected values of normalized SIF.

He and Hutchinson [2] provided solutions for the AFPS specimen which have been used for comparison with a two-dimensional model in Abaqus FEA. The current analysis shows good agreement with the literature solutions over the full range of crack depths considered. Figure 5 shows the current FEA results for various crack depths and crack offset ratios (*c*/*W*). The percent differences are found to be small for all cases of *a*/*W* and *c*/*W*, within 1%.

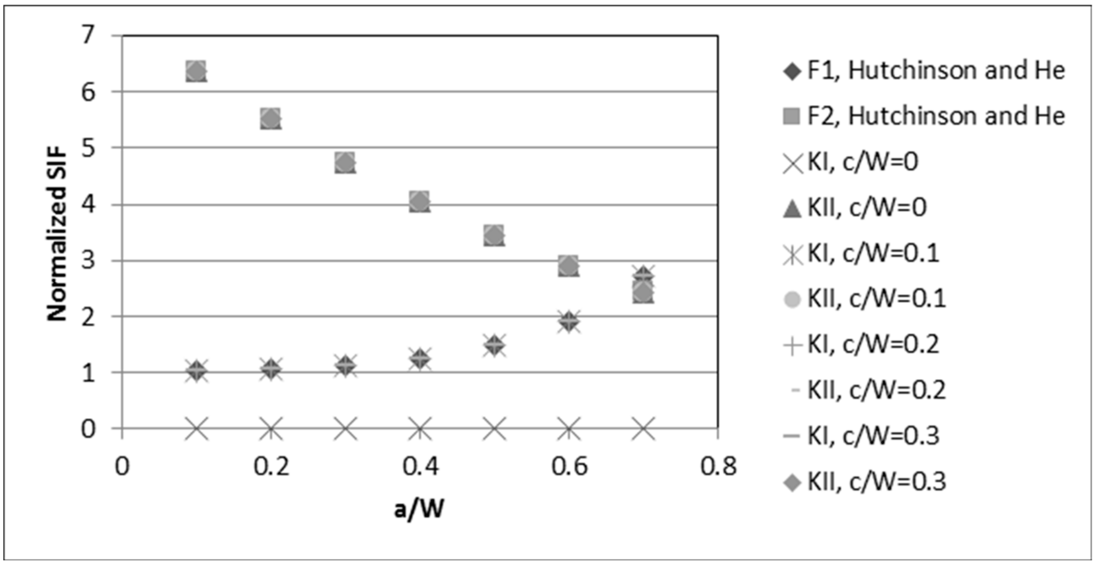

Figure 5. 2D FEA comparison with literature results.

3.4. Results for c = 0

Note for the case of $c = 0$, the K_I, T_{11}, and T_{33} are all zeros due to the antisymmetric feature. The results for K_{II} and K_{III} are shown in Figures 6 and 7, respectively.

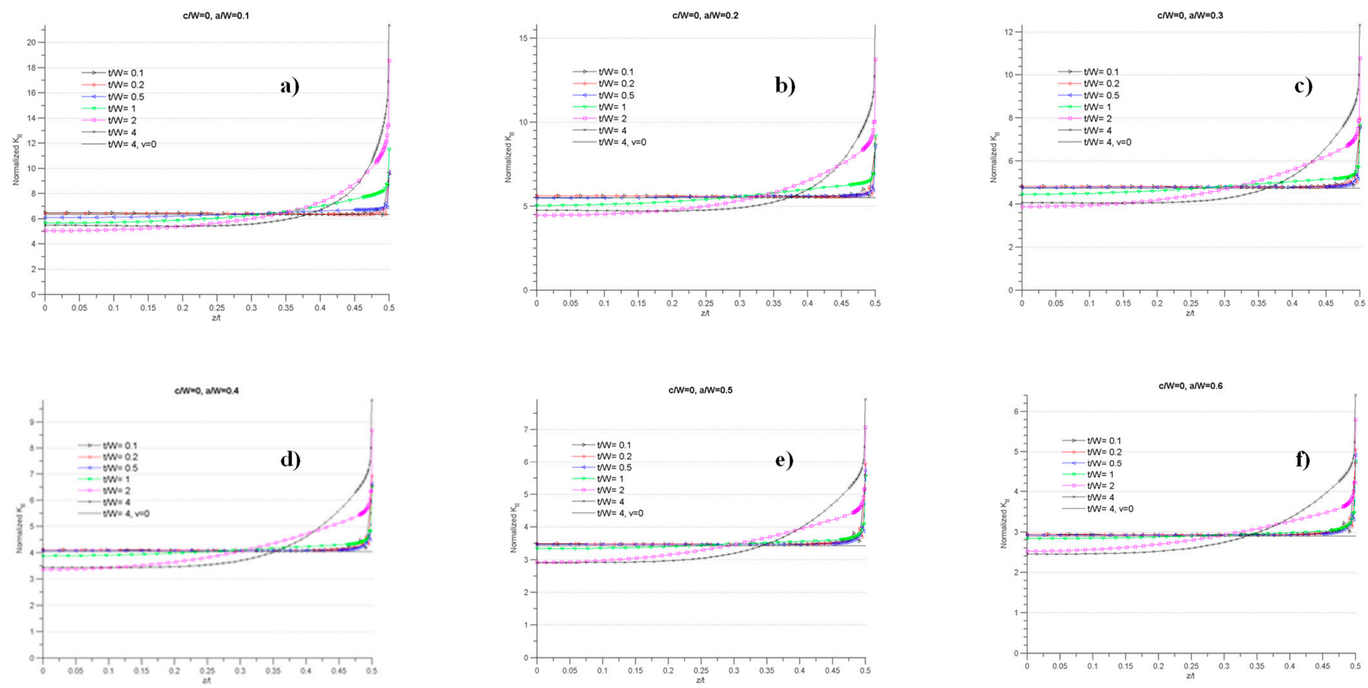

Figure 6. Normalized K_{II} for (**a**) *a*/*W* = 0.1, (**b**) *a*/*W* = 0.2, (**c**) *a*/*W* = 0.3, (**d**) *a*/*W* = 0.4, (**e**) *a*/*W* = 0.5, and (**f**) *a*/*W* = 0.6.

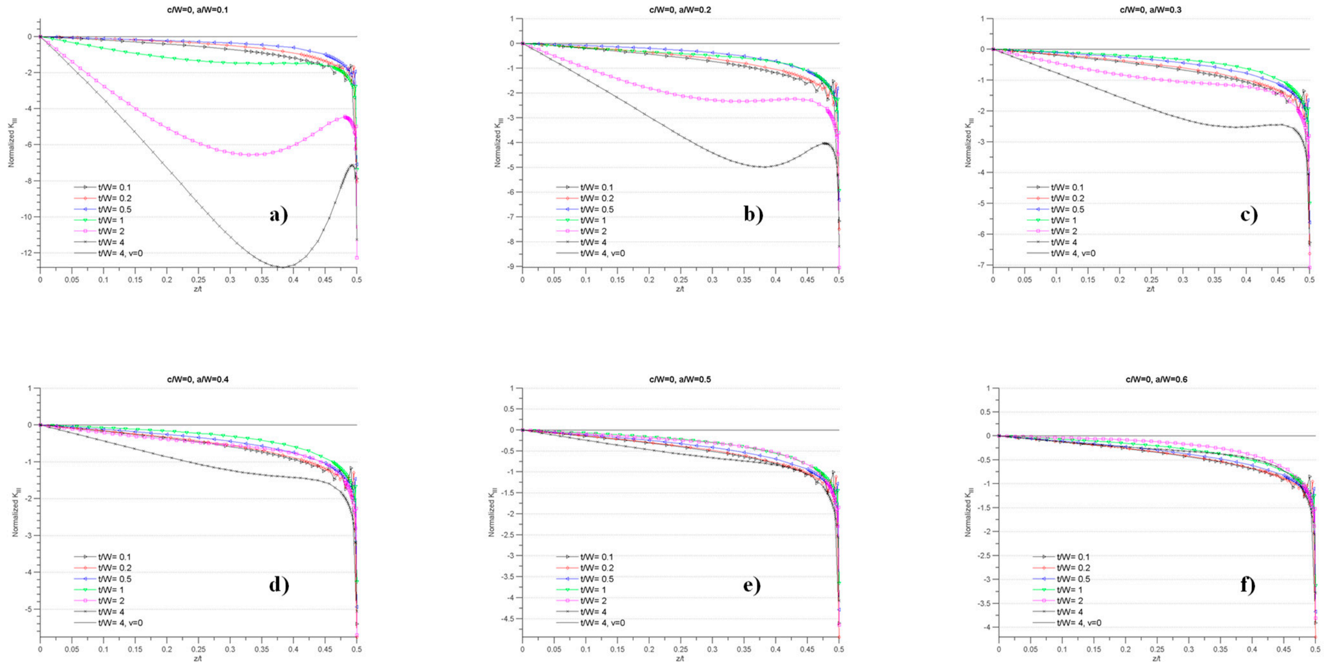

Figure 7. Normalized K_{III} for (**a**) a/W = 0.1, (**b**) a/W = 0.2, (**c**) a/W = 0.3, (**d**) a/W = 0.4, (**e**) a/W = 0.5, and (**f**) a/W = 0.6.

Of the six thickness cases considered, the results can be split into two groups: thick plates and thin plates. The cases of t/W = 0.1, 0.2, and 0.5, can be considered as thin plates, and show only minor variation in K_{II} value through-thickness, corresponding well to the 2D literature solutions. From Figure 6a–f it can be seen that the thin plate cases are typically only a few percent from the literature solution at the mid plane. The K_{II} values of these thin plates are fairly constant and positive in value, through the thickness, with a steep increase very close to the free edge (z/t = 0.5).

The K_{III} values have a different trend, as shown in Figure 7a–f, with all cases having a value of 0 at the mid plane and steadily decreasing (increasing magnitude in negative direction) towards the free edge, where, very close to the free edge, the values appear to approach infinity. The trends of through-thickness SIF variation of K_{II} and K_{III} do not appear to change appreciably with varying a/W. The value of K_{II} decreases significantly with increasing a/W, while the value of K_{III} only decreases slightly.

The plates which can be considered to represent thick cases, t/W = 1.0, 2.0, and 4.0, show significantly more variation through-thickness in both K_{II} and K_{III}. The value of K_{II} tends to be significantly lower (10–20%) for the two thickest cases across all values of a/W. The case of the square plate (t/W = 1.0) shows intermediate behaviour between the extreme thickness cases, and the thin-plate behaviour. The mid-plane results for the square case show a large deviation (10%) from the literature solutions for shallow cracks but show only minor deviation (2%) for deep cracks. A defining feature of the K_{II} variation for these so-called thick plates is a noticeable increase in magnitude from a position around z/t = 0.3 to the free edge. For t/W = 1.0, this increase is minor, but for the two thicker cases of t/W = 2.0 and 4.0, the values increase significantly for the area near the free surface. For K_{III}, the amount of the variation of through-thickness values between the thin plates, and even the square case, is dwarfed at shallow crack depths by the extreme variation of K_{III} for the two thickest cases. For the shallow cracks of a/W < 0.4, the thick cases show a sharp increase in magnitude K_{III}, which peaks at around z/t = 0.3 for t/W = 2.0, and z/t = 0.375 for t/W = 4.0. The values of K_{III} are all large enough in magnitude that neglecting to take these into account would be a significant oversight.

3.5. Results for c = 0.1

Next, typical results of fracture mechanics parameters for a/W = 0.1 and 0.5 with varying t/W ratios of 0.1, 0.2, 0.5, 1, 2, and 4 are presented in this paper. Figure 8 shows the results for K_I, K_{II}, K_{III}, and Figure 9 illustrates T_{11} and T_{33}, respectively. In Figure 8a,d, the mode I SIF values show a general trend of decreasing values of K_I as the position through-thickness approaches the free surface. This trend of the K_I value dropping towards the free surface appears for all thickness cases and for all considered crack depths. For the case of thin specimens (t/W < 1.0), the values of K_I are all very close and show similar through-thickness variation. With increasing thickness appears to be a decreasing value of K_I, an effect that is most pronounced for the shallowest crack (a/W = 0.1) case. The two thickest cases (t/W = 2.0, 4.0) show significantly reduced values of K_I located at positions of z/t = 0.25 up to the free surface when compared with the values of the thinner cases. The effect of increasing thickness appears to be most significant at low values of a/W.

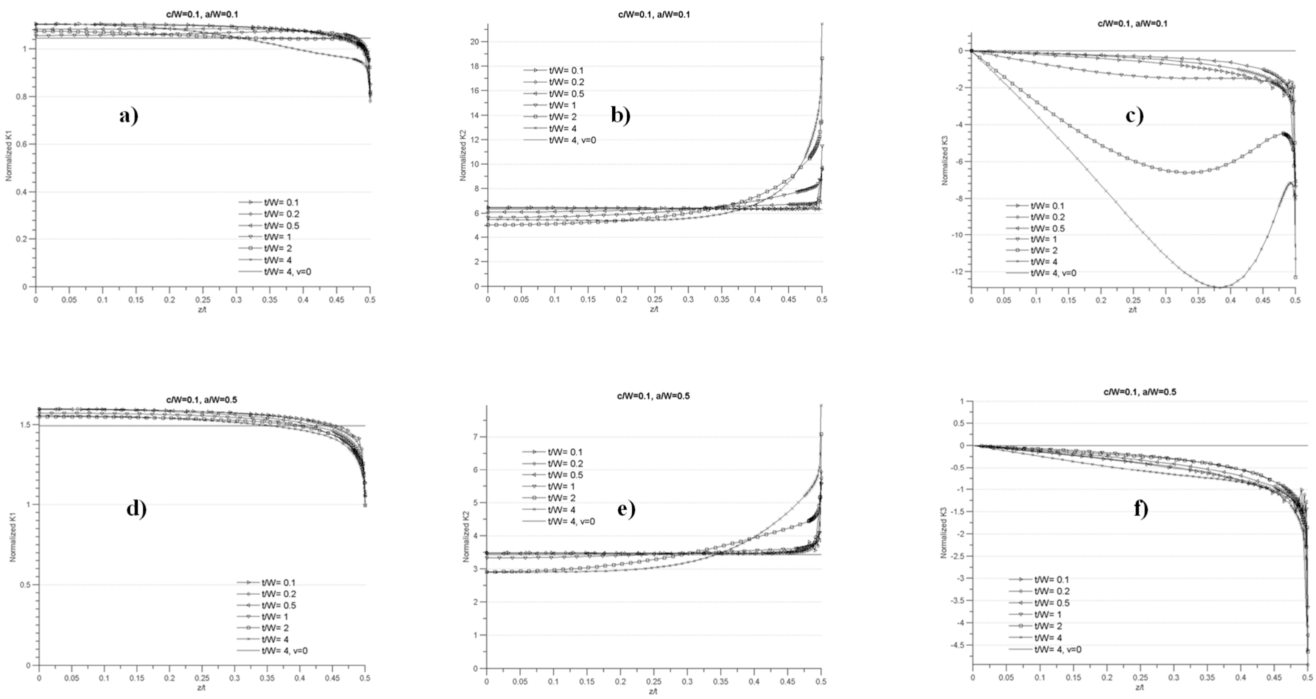

Figure 8. Results for a/W = 0.1, (**a**) K_I, (**b**) K_{II} (**c**) K_{III}, and a/W = 0.5, (**d**) K_I, (**e**) K_{II}, and (**f**) K_{III}.

In Figure 8b,c,e,f, the SIFs associated with the mode II loading, K_{II} and K_{III}, are shown. Comparison with the previous results calculated in the pure mode II result (i.e., FPS specimen, with c = 0), obtained in Section 3.4 is also made, and similar trends are observed.

The T_{11} and T_{33} results are shown in Figure 9. The trends of T-stress variation through-thickness, and with respect to t/W ratio, are seen to be consistent with the trends identified in Jin and Wang [3]. The value of T_{11} is negative for $a/W \leq 0.3$, and positive for the deeper cracks where a/W > 0.3. The trends of variation through-thickness appear mostly independent of a/W, and the value of T_{11} is, for the most part, constant across the thickness. The values of T_{11} are observed to increase as thickness decreases, at the midplane and most of the through-thickness locations. The cases of thicker specimens (t/W > 1.0) show increasing values of T_{11} for the locations from z/t = 0.3 up to the free surface.

The plots of T_{33} show trends that can be described more easily. Thickness appears to inversely correlate to T_{33} value, where the thinner specimens have a larger magnitude of T_{33}. T_{33} increases with increasing a/W ratio, which could be attributed to the fact that the a/W ratio is not considered in the normalizing functions. The value of T_{33} is also observed to decrease as the position approaches the free surface, with the thicker specimens showing a decrease beginning at higher values of *z/t*, while thinner specimens show a decrease which starts to become evident at lower values of *z/t*.

Overall, the trends in the parameters associated with the mode I loading, K_I, T_{11}, and T_{33}, are observed to have significant through-thickness variation, and each parameter has its own trend with respect to crack depth and thickness ratios.

Note that the results shown in Sections 3.3 and 3.4 should be considered suitable within the range of $0 \leq z/t < 0.5$. When $z/t \to 0.5$, there will be a 3D corner/vertex singularity, different from the standard $1/\sqrt{r}$ singularity, which was not considered in the present work.

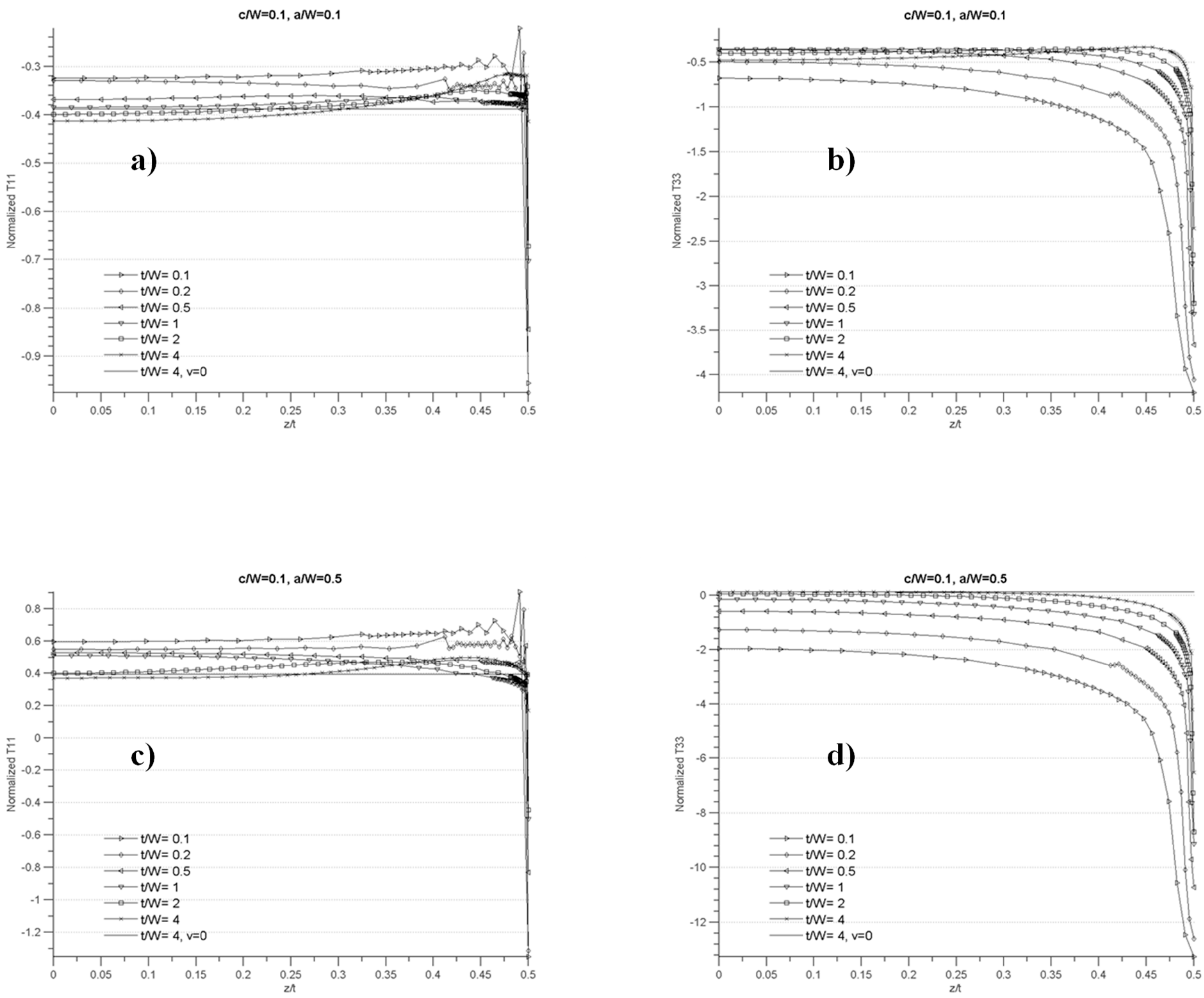

Figure 9. Results for *a/W* = 0.1, (**a**) T_{11}, (**b**) T_{33} and for a/W = 0.5, (**c**) T_{11}, and (**d**) T_{33}.

4. Plastic Zone Analysis

Of interest in fracture problems is the size and shape of the plastic zone (PZ), which is defined for our purpose as the boundary between elastic and plastic material behaviour. The plastic zone is found by isolating the region subjected to stress equal to or greater than an effective yield stress. PZ size is used as an indicator of whether LEFM parameters can adequately describe the stress state around the crack tip. Using single- and two-parameter fracture mechanics methods, the size and shape of the plastic zone can be estimated either with or without the *T*-stress effect under mixed mode loading.

In this section, the SIF and *T*-stress results extracted from the current FEA are used to predict the size and shape of the plastic zone. The impact of including the *T*-stress term on the plastic zone was studied, as well as the plastic zone variation through-thickness for a variety of plate thickness.

A method for tracing the boundary of the plastic zone was created and verified against the previous methods of Nazarali and Wang [13]. Current FEA results were used to plot the plastic zone size and shape at various locations through the specimen's thickness.

4.1. Calculating and Plotting the Plastic Zone from LEFM Parameters

The William's series expansion for the stress around a crack tip calculates the stress components, in polar coordinates, at a distance r from the crack tip and at angle θ. In mixed-mode loading, the mode I, mode II, and mode III stress contributions, together with T_{11} and T_{33}, can be obtained from William's series expansion. The contributions of mode I loading are

$$\begin{aligned}
\sigma_{11}(r,\theta) = &\ \frac{K_I}{\sqrt{2\pi r}} cos\left(\frac{\theta}{2}\right)\left[1 - sin\left(\frac{\theta}{2}\right)sin\left(\frac{3\theta}{2}\right)\right] + T_{11} \\
\sigma_{22}(r,\theta) = &\ \frac{K_I}{\sqrt{2\pi r}} cos\left(\frac{\theta}{2}\right)\left[1 + sin\left(\frac{\theta}{2}\right)cos\left(\frac{3\theta}{2}\right)\right] \\
\sigma_{12}(r,\theta) = &\ \frac{K_I}{\sqrt{2\pi r}} cos\left(\frac{\theta}{2}\right)sin\left(\frac{\theta}{2}\right)cos\left(\frac{3\theta}{2}\right) \\
\sigma_{33}(r,\theta) = &\ v\left(\frac{K_I}{\sqrt{2\pi r}} cos\left(\frac{\theta}{2}\right)\left[1 - sin\left(\frac{\theta}{2}\right)sin\left(\frac{3\theta}{2}\right)\right] + \sigma_{22}\right) + T_{33}
\end{aligned} \tag{10}$$

For mode II loading, the stress state can be described in polar coordinates by the following [15]:

$$\begin{aligned}
\sigma_{11}(r,\theta) = &\ -\frac{K_{II}}{\sqrt{2\pi r}} sin\left(\frac{\theta}{2}\right)\left[2 + cos\left(\frac{\theta}{2}\right)cos\left(\frac{3\theta}{2}\right)\right] \\
\sigma_{22}(r,\theta) = &\ \frac{K_{II}}{\sqrt{2\pi r}} sin\left(\frac{\theta}{2}\right)\left[cos\left(\frac{\theta}{2}\right)cos\left(\frac{3\theta}{2}\right)\right] \\
\sigma_{12}(r,\theta) = &\ \frac{K_{II}}{\sqrt{2\pi r}} cos\left(\frac{\theta}{2}\right)\left[1 - sin\left(\frac{\theta}{2}\right)sin\left(\frac{3\theta}{2}\right)\right] \\
\sigma_{33}(r,\theta) = &\ v(\sigma_{11} + \sigma_{22})
\end{aligned} \tag{11}$$

where v is Poisson's ratio.

For pure mode III, the stress state can be described as follows:

$$\begin{aligned}
\sigma_{13}(r,\theta) = &\ -\frac{K_{III}}{\sqrt{2\pi r}} sin\left(\frac{\theta}{2}\right) \\
\sigma_{23}(r,\theta) = &\ \frac{K_{III}}{\sqrt{2\pi r}} cos\left(\frac{\theta}{2}\right)
\end{aligned} \tag{12}$$

Applying the principle of superposition for both modes, the total stress can be calculated:

$$\sigma_{ij}{}^{(total)} = \sigma_{ij}{}^{(I)} + \sigma_{ij}{}^{(II)} + \sigma_{ij}{}^{(III)} \tag{13}$$

The stress components from Equation (13) are substituted into von Mises' yield criterion. The plastic zone radius is extracted using the process described in Cohen [16]; an effective SIF, K_{eff}, is used to normalize the plastic zone, and includes the mode I component as follows:

$$K_{eff} = \sqrt{K_I^2 + K_{II}^2} \tag{14}$$

The plastic zone is normalized using the values only at the midplane; in this way, the through-thickness variation of the plastic zone can be clearly seen.

By using the components defined by the Williams' expansion, a yield criterion can be applied—in this case, von Mises' yield criterion. The effective von Mises' stress is given by:

$$\sigma_e = \sqrt{\frac{(\sigma_{11} - \sigma_{22})^2 + (\sigma_{22} - \sigma_{33})^2 + (\sigma_{33} - \sigma_{11})^2 + 6\left(\sigma_{12}^2 + \sigma_{23}^2 + \sigma_{31}^2\right)}{2}} \tag{15}$$

Assuming an arbitrary value of yield stress, the Williams expansion terms in Equations (10)–(12) can be inserted into Equation (13) and subsequently equated to the von Mises' yield criterion (Equation (15)). This expression can be used to calculate r, in terms of θ, around the crack tip for a given yield stress value.

In order to determine r, the radius that defines the boundary between elastic and plastic behaviour, a symbolic solver was implemented in MATLAB to calculate the plastic zone for the FEA results previously presented. The function used in MATLAB was *vpasolve*, and the variable r, the radial distance from the crack tip in Equations (10)–(12), was assigned as a symbolic variable in MATLAB [17]. Non-normalized SIF values were substituted into Equation (8), and r was found for the full range of θ at several locations through the thickness. For pure mode II loading, the plastic zone was normalized as a function of K and yield stress:

$$Normalized\ plastic\ zone\ radius\ R_p = \frac{r}{\frac{1}{\pi}\left[\frac{K_{II}}{\sigma_{YS}}\right]^2} \tag{16}$$

To show the relative size of the plastic zone at various locations through the specimen's thickness, the value of K_{II} at the mid plane was used to normalize all values of R_p for each of the different through-thickness cases. The value of K_{III} was found to be zero at the mid plane for all values of t/W, so the impact of its inclusion in calculating the PZ can be clearly seen. On the first plastic zone plot, the location of the crack line is shown for illustration purposes.

In order to confirm the current calculation method, some baseline cases were compared with values obtained from using the equations provided by Nazarali and Wang [10]. The full set of equations is given in [10], and the equations are valid for mode I and II loading cases. Figure 10 shows the plastic zones for pure mode II and mode III loading cases obtained using the present procedure and the one from Nazarali and Wang [7].

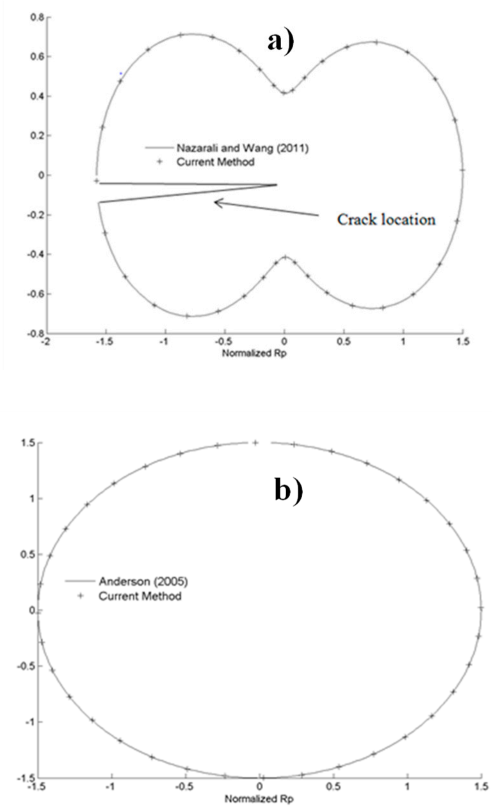

Figure 10. Plastic zone verification of a pure mode II case (**a**) and a pure mode III case (**b**).

4.2. Plastic Zone Results for c = 0

From the produced plots of the normalized plastic radius, as shown in Figure 11, it is initially noticeable that the behaviour can again be grouped into two types: thick and thin. The considered specimens for the plastic zone analysis have t/W ratios of 0.1, 0.5, 1.0, 2.0, and 4.0. The case of t/W = 0.2 has been excluded for space considerations, and it is expected to be almost identical to the case of t/W = 0.1. In Figure 11, the results for three t/W ratios (0.1, 1.0, and 4.0) were shown.

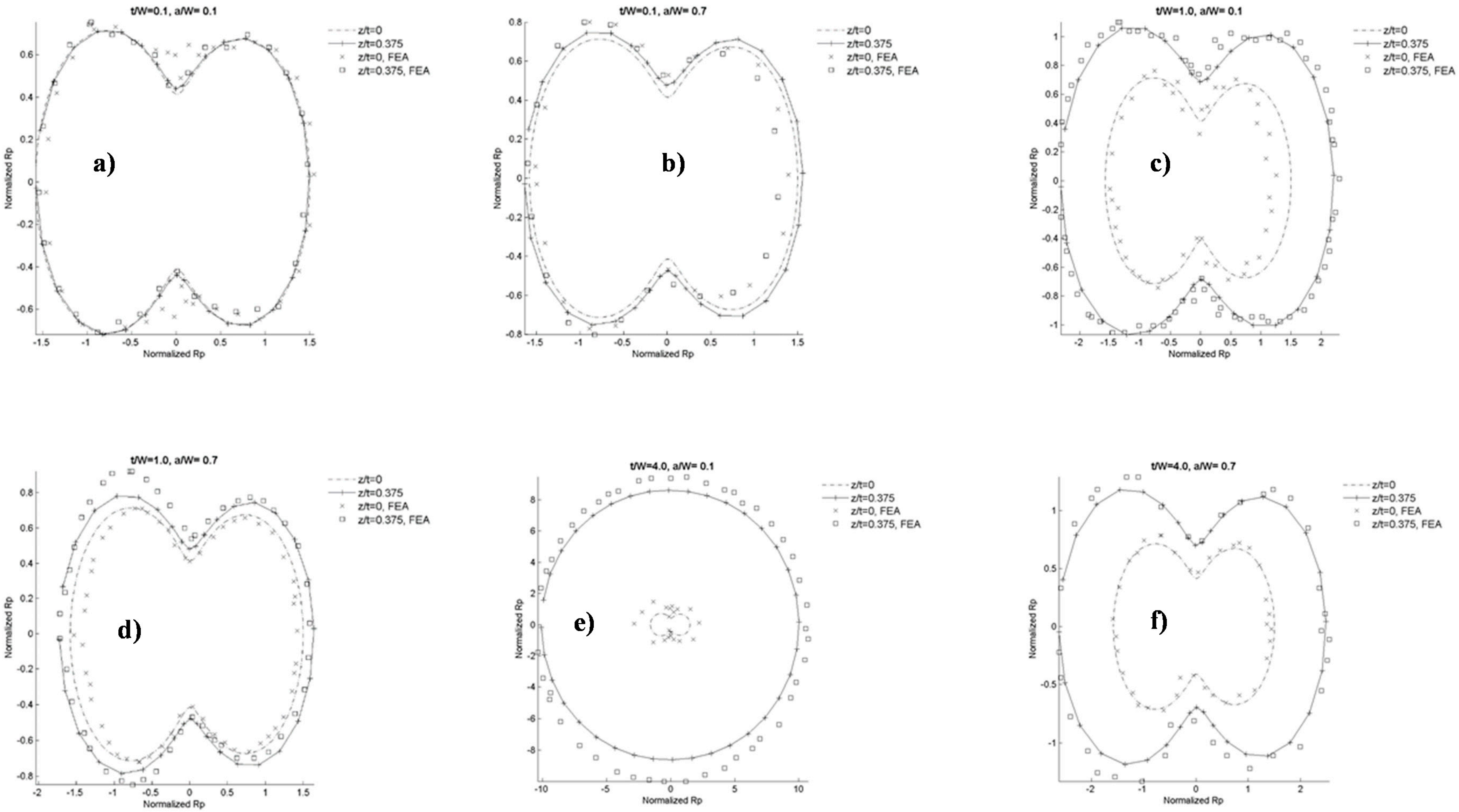

Figure 11. Plastic zone comparison for (**a**) $t/W = 0.1$, $a/W = 0.1$, (**b**) $t/W = 0.1$, $a/W = 0.7$, (**c**) $t/W = 1.0$, $a/W = 0.1$, (**d**) $t/W = 1.0$, $a/W = 0.7$, and (**e**) $t/W = 4.0$, $a/W = 0.1$, (**f**) $t/W = 4.0$, $a/W = 0.7$.

When comparing the plastic zones, for all cases, the smallest plastic zone (through-thickness) was located at the mid plane, and the plastic zone radius increased at all positions towards the free surface. The value of K_{III} always reached zero at the mid plane, so the plastic zone in the middle of the plate can be expected to resemble that of pure mode II loading. The relative increase in plastic zone size was small for the thin (t/W = 0.1, 0.5) plates considered, but was significant for the thicker cases. The thin plates showed a plastic zone which stayed at a fairly constant size in the shape expected of pure mode II loading. The case of t/W = 1.0 (see Figure 11c,d) showed an increased plastic zone at locations approaching the free surface, still in the shape of pure mode II loading. The size increase (from the mid plane) of the plastic zone at outer positions appeared to decrease with increasing a/W, where shallower cracks had larger variations in plastic zone size than deep cracks.

As might be expected from the significant K_{III} variations seen in Figure 7, the thickest cases had the largest plastic zone variations of through the specimen's thickness. For t/W = 4.0, Figure 11e,f shows an increased plastic zone size, with circular shape, at the location close to the free edge. This change in shape and increase in size corresponded with the high value of K_{III} at that location through the specimen's thickness. This effect is most noticeable in the shallow-crack case of the thickest plate considered, t/W = 4.0, where the plastic zone at the mid plane appeared to be just a fraction of that at the near-surface point (z/t = 0.375). At this near-surface point, the plastic zone appeared almost perfectly round, and represented a high amount of mode III contribution.

The calculated plastic zone sizes described using the William's expansion and the von Mises' yield criterion provided results showing large variations of plastic zone size and shape through-thickness. In order to verify that these predicted values were consistent with the stress results from elastic FEA, the PZ shape and size were estimated from the stress contour and compared with the prediction for some typical cases.

Image analysis was used to gather data from the FEA stress contours. The FEA-extracted plastic zone data was normalized using the same method and values as used for the predicted plastic zones. Some typical thickness cases were considered—t/W = 0.1,1.0, and 4.0—for the cases of crack depth extremes, a/W = 0.1 and 0.7. In these figures, the number of data points shown for the FEA-extracted results was reduced for clarity.

In the current analysis, for specimens with relatively small plastic zones, for example, mid-plane at shallow cracks, the plastic zone could be confined to be within a single element. This was not an ideal situation, as the built-in stress contour within Abaqus must be used to approximate the boundary. As seen in the comparison case, the plastic zone estimated by the SIF solutions showed good agreement with the FEA images for all typical cases. The thin case, t/W = 0.1, had little variation in through-thickness for both thick and thin cracks. The resulting plots, from Figure 11, show good correlation with size and shape of the extracted and calculated plastic zones. There was some overlap of the FEA-extracted plastic zones for the two positions in each of the two thin cases, and this was attributed to inaccuracies in the extraction method and coarseness of the contour refinement.

The square (t/W = 1.0) specimen showed very good agreement between the calculated and extracted values for both crack depth ratios considered. Similar agreement was seen with the thick case of t/W = 4.0; however, it appeared that the FEA-extracted values were slightly larger than the calculated values for the shallow crack (a/W = 0.1) case. This apparent difference could be attributed to contour coarseness or even mesh coarseness in the area surrounding the crack. The deep-crack case showed better agreement with the calculated values and supported the predicted values. Overall, the comparison cases showed that the plastic zone size and shape, as predicted by the current calculation method, was consistent with results from the FEA stress contours.

4.3. Plastic Zone Results for c = 0.1

In the current analysis, two plastic zone size predictions are made, the first calculated including the effects of only the three SIFs and the second including all SIF and T-stress values. The plastic zones calculated including only SIF are presented in Figure 12, while the plastic zones calculated using all SIF and *T*-stress terms are in Figure 13. Here the results for the thin specimen case, *t/W* = 0.1, with two different *a/W* ratios (0.1 and 0.5) are shown.

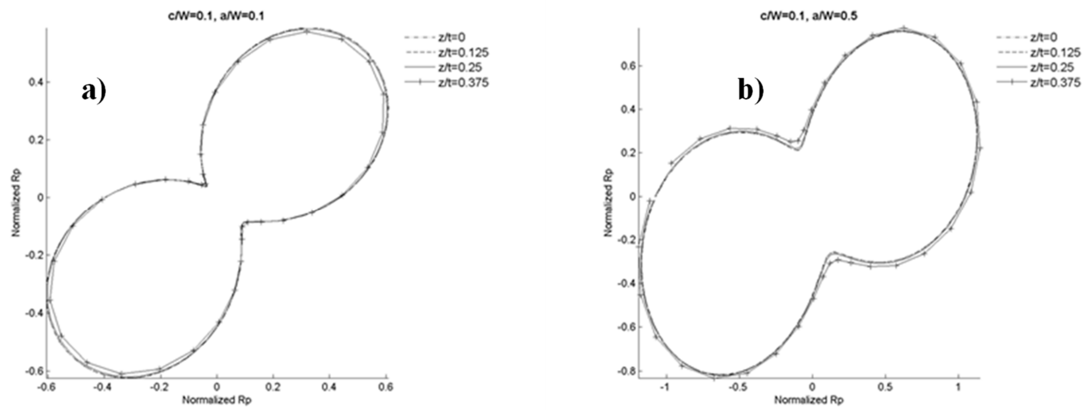

Figure 12. Plastic zone based on SIF only; (**a**) *a/W* = 0.1, *t/W* = 0.1, (**b**) *a/W* = 0.5, *t/W* = 0.1.

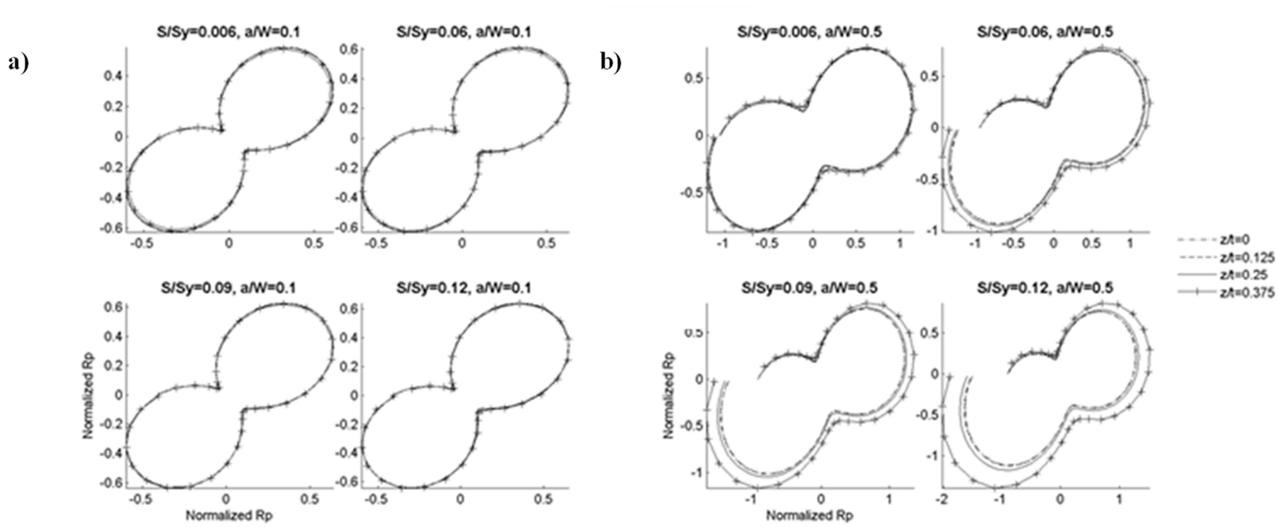

Figure 13. Plastic zone based on SIF and *T*-stress; (**a**) *a/W* = 0.1, *t/W* = 0.1, (**b**) *a/W* = 0.5, *t/W* = 0.1.

The plastic zone plots calculated using just the three SIFs (Figure 12) show that the mixed-mode effect is seen to influence the shape of the plastic zone, depending on the mixed-mode ratio. The proportion of K_{II} to K_I, the mixed-mode ratio, determines the shape of the plastic zone at the midplane (where $K_{III} = 0$). The variation of all three SIFs' through-thickness influences the plastic zone by apparently increasing the size of the plastic zone at locations approaching the free surface.

Considering all SIFs together with *T*-stresses, the influence of *T*-stress can be seen in the shape of the plastic zone, which is similar to, albeit less exaggerated than, that observed by Nazarali and Wang [13]. The influence of *T*-stress can be subtle or extreme, as seen in Nazarali and Wang [13], depending on the relative *T*-stress and yield stress values. In this way, the effect of the relative *T*-stress can be studied, as previous researchers have done. To provide some means of evaluating the increased effect that *T*-stress has on the plastic zone size and shape, a loading level ratio is introduced as

$$Load\ level = \frac{\sigma^{nom}}{\sigma_{YS}}$$

In the current analysis, the values of load level considered are 0.006 (a low-loading scenario), 0.06, 0.09, and 0.12 (a high-loading case), providing a good range of T-stress effects that can be observed. The ratio S/Sy used in the plastic zone plots in Figure 13 refers to the load level ratio σ^{nom}/σ_{YS}.

By comparing the plastic zone predictions calculated with and without T-stress, the influence of T-stress can be shown. At low load levels, the value of T-stress, with respect to yield stress, is low, and the plastic zone contribution is small. The plastic zone plots for relatively low load levels (σ^{nom}/σ_{YS} = 0.006, 0.06) show plastic zones consistent with those predicted without T-stress effects. It is clear that for moderate- to larger-scale yielding, the T-stress effects need to be included.

5. Summary and Conclusions

From the plots of the results, some key observations can be made about the inclusion of K_{III} in the fracture analysis of the FPS specimen. Primarily, it can be seen that the K_{III} influence on pure mode II loading cannot be ignored and can influence PZ size and shape greatly. The coupling of K_{II} and K_{III} is caused by Poisson's ratio's effects at the free surface, which can be significant for thick specimens. This is seen most easily in the exaggerated case shown in Figure 11e (t/W = 4.0, a/W = 0.1), where a large magnitude of K_{III} is seen to greatly affect the plastic zone size and shape, resembling a circular shape, similar to that expected of a pure mode III loading scenario. The trends seen in the results indicate that thick plates containing shallow cracks are most affected by the influence of K_{III}. The through-thickness comparison of SIF variation also showed an interesting trend, with some extreme cases showing significant variation in plastic zone size and shape at different locations through the specimen's thickness.

Another key observation is that the amount of through-thickness variation of K_{II} appeared to be a function of the thickness of the plate. The trends identified show an increasing K_{II} variation for increased plate thickness. For the thicker cases ($t/W > 1.0$), it was observed that the value of K_{II} at the mid plane was lower than the literature solution but increased to higher values closer to the free surface.

To see the total effect of finite-thickness considerations on the pure mode II loading case, the PZ size and shape were used as an indicator of crack tip stress state. It was observed that the through-thickness variation in the SIFs (increasing magnitude in positive K_{II} and negative K_{III}) had a tendency to increase PZ size. Inspection of the von Mises' yield criterion showed that, in the absence of K_I, the K_{III} stress contributions served to increase the effective stress, which in turn increased the radius of the predicted plastic zone. The produced PZ plots show that, for relatively thick plates ($t/W \geq 1.0$), the plastic zone is not of constant through the specimen's thickness and enlarges at locations approaching the free surface.

The main conclusion that can be drawn from the pure mode II analysis of the FPS specimen is that the inclusion of 3D effects can have a very large effect on the plastic zone and stress field surrounding a crack and must be considered. Of the cases considered in this analysis, the relatively thick ($t/W > 1.0$) plate specimens were affected most when shallow cracks were present, with the largest values of K_{III} and the biggest amount of through-thickness variation. What this could mean, in practical terms, is that the critical area to consider in these shallow-crack thick-plate bodies is not necessarily located at either the mid- or edge plane, but rather at some location between. This conclusion is counter to the results for K_I in pure mode I specimens [3], which showed thick plates in good agreement with a plane strain 2D reference solution. The current results suggest that applying a similar assumption to mode II specimens, when considering mode III influence, would be incorrect.

The current analysis also suggests that for thin plates ($t/W < 1.0$), the variation of through-thickness appears to be less significant than for thick plates, and the inclusion of the K_{III} term has a less pronounced effect. This conclusion is arrived at after inspection of the plastic zone plots, which can be used qualitatively to estimate the influence of each mode's

SIF. Thin FPS fracture specimens appear to be consistent with the 2D reference solutions, and test results could be interpreted using these solutions with reasonable accuracy.

The fracture parameter solutions obtained in this work will be very useful for fracture toughness testing of FPS specimens. The results of the plastic zone analysis performed in this work provide a clear illustration of the 3D effects on fracture specimens of varying thicknesses undergoing pure mode II loading.

From the analysis of the AFPS specimen, it is found that finite thickness effects have significant effect on the fracture mechanics parameters. For mixed-mode I/II loading, the finite thickness effect is present at all thicknesses. For thin specimens, T-stress magnitudes are large approaching the free surface, enlarging the plastic zone greatly. At the other end of the spectrum, thick specimens do not see the same amount of T-stress effect, but large K_{II} and K_{III} values cause enlarged plastic zones at locations between the midplane and free edge. The current findings show that the plastic zone is also affected by all three SIFs and two T-stresses.

The findings from the current analysis show that using 2D solutions to interpret fracture specimens undergoing mixed-mode loading will not adequately describe the stress at the crack. It is necessary to consider the finite thickness effects on the specimen, as well as the crack tip constraint effect from the T-stress.

Author Contributions: Conceptualization, X.W.; methodology, M.C. and X.W.; software, M.C.; validation, M.C. and X.W.; formal analysis, M.C.; investigation, M.C.; resources, X.W.; data curation, M.C.; writing—original draft preparation, M.C.; writing—review and editing, X.W.; visualization, M.C.; supervision, X.W.; project administration, X.W.; funding acquisition, X.W. All authors have read and agreed to the published version of the manuscript.

Funding: This research was funded by the Natural Science and Engineering Research Council (NSERC) of Canada grant number (RGPIN-2020-06550).

Institutional Review Board Statement: Not applicable.

Informed Consent Statement: Not applicable.

Data Availability Statement: Not applicable.

Conflicts of Interest: The authors declare no conflict of interest.

References

1. He, M.Y.; Cao, H.C.; Evans, A.G. Mixed-mode fracture: The four-point shear specimen. *Acta Metall. Mater.* **1990**, *38*, 839–846. [CrossRef]
2. He, M.Y.; Hutchinson, J.W. Asymmetric four-point crack specimen. *J. Appl. Mech.* **2000**, *67*, 207–209. [CrossRef]
3. Jin, Z.; Wang, X. Characteristics of crack front stress fields in three-dimensional single edge cracked plate specimens under general loading conditions. *Theor. Appl. Fract. Mech.* **2015**, *77*, 14–34. [CrossRef]
4. Kwon, S.W.; Sun, C.T. Characteristics of three-dimensional stress fields in plates with a through-the-thickness crack. *Int. J. Fract.* **2000**, *104*, 289–314. [CrossRef]
5. Nakamura, T.; Parks, D.M. Antisymmetrical 3-D stress field near the crack front of a thin elastic plate. *Int. J. Solids Struct.* **1989**, *25*, 1411–1426. [CrossRef]
6. Jin, P.; Liu, Z.; Wang, X.; Chen, X. Three-dimensional analysis of mixed mode compact-tension-shear (CTS) specimens: Stress intensity factors, T-stresses and crack initiation angles. *Theor. Appl. Fract. Mech.* **2022**, *118*, 103218. [CrossRef]
7. Betegon, C.; Hancock, J.W. Two-parameter characterization of elastic-plastic crack tip fields. *ASME J. Appl. Mech.* **1991**, *58*, 104–110. [CrossRef]
8. O'Dowd, N.P.; Shih, C.F. Family of crack tip fields characterised by a triaxiality parameter—I, structure of fields. *J. Mech. Phys. Solids* **1991**, *39*, 989–1015. [CrossRef]
9. Wang, X. Elastic T-Stress for cracks in test specimens subjected to non-uniform stress distributions. *Eng. Fract. Mech.* **2002**, *69*, 1339–1352. [CrossRef]
10. Liu, Z.; Wang, X.; Tang, J.; Deng, C.; Zhao, H.; Chen, X. The effects of in-plane and out-of-plane constraints on JR curves for X80 steel: A study using clamped SENT specimens. *Eng. Fract. Mech.* **2019**, *206*, 342–358. [CrossRef]
11. Liu, Z.; Wang, X.; Miller, R.E.; Hu, J.; Chen, X. Ductile fracture properties of 16MND5 bainitic forging steel under different in-plane and out-of-plane constraint conditions: Experiments and predictions. *Eng. Fract. Mech.* **2021**, *241*, 107359. [CrossRef]
12. Liu, Z.; Wang, X.; Miller, R.E.; Jin, P.; Shen, Y.; Chen, X. Determination of R-curves for thermal aged 16MND5 bainitic forging steel using 3D constraint-based fracture mechanics. *Theor. Appl. Fract. Mech.* **2021**, *116*, 103084. [CrossRef]

13. Nazarali, Q.; Wang, X. The effect of T-stress on crack-tip plastic zones under mixed-mode loading conditions. *Fatigue Fract. Eng. Mater. Struct.* **2011**, *34*, 792–803. [CrossRef]
14. *Dassault Systèmes/SIMULIA Modeling Fracture and Failure with Abaqus*; Dassault Systèmes: Providence, RI, USA, 2013.
15. Anderson, T.L. *Fracture Mechanics: Fundamentals and Applications*, 3rd ed.; CRC Press: Boca Raton, FL, USA, 2005.
16. Cohen, M. 3D Mixed-Mode Fracture of the 4-Point Shear Specimen. Master's Thesis, Carleton University, Ottawa, ON, Canada, 2015.
17. MathWorks. *MATLAB User Manual*; MathWorks: Natick, MA, USA, 2015.